PHYSICS

Probing the in-plane liquid-like behavior of liquid crystal elastomers

Haruki Tokumoto[1†], Hao Zhou[2†], Asaka Takebe[1], Kazutaka Kamitani[3], Ken Kojio[3], Atsushi Takahara[3], Kaushik Bhattacharya[2*], Kenji Urayama[1*]

When isotropic solids are unequally stretched in two orthogonal directions, the true stress (force per actual cross-sectional area) in the larger strain direction is typically higher than that in the smaller one. We show that thiol-acrylate liquid crystal elastomers with polydomain texture exhibit an unusual tendency: The true stresses in the two directions are always identical and governed only by the area change in the loading plane, independently of the combination of imposed strains in the two directions. This feature proves a previously unidentified state of matter that can vary its shape freely with no extra mechanical energy like liquids when deformed in the plane. The theory and simulation that explain the unique behavior are also provided. The in-plane liquid-like behavior opens doors for manifold applications, including wrinkle-free membranes and adaptable materials.

INTRODUCTION

Rubbers (elastomers) have high reversible extensibility and very low elastic modulus that originate from the entropic elasticity of polymer chains (*1*–*3*). Introducing liquid crystallinity to elastomers results in a unique class of soft solid material called liquid crystal elastomer (LCE) (*4*). LCE is obtained by loosely cross-linking the main-chain LC polymers with the mesogens being part of the linear chains or the side-chain LC polymers with the mesogens in the parts dangling from a nonmesogenic polymer backbone (*5*, *6*). Both types of LCE exhibit a fascinating stimulus-response property owing to the coupling of LC order and rubber elasticity: The LCEs deform in response to a variation in the LC order as the LC order induces the orientation of polymer network strands along the director (principal direction of LC anisotropy). This property enables the actuation of the elastomers by various types of stimulus such as temperature change and electric, magnetic, and optical fields, each of which can drive a variation in the LC order. Various complex deformations can also be programmed by spatially controlling the director configuration in LCEs (*7*). LCEs are therefore attracting considerable attention as a promising material for soft actuator and bioinspired mechanical devices.

The coupling of LC order and rubber elasticity also results in an unusual mechanical property that is called "soft elasticity." In this well-studied phenomenon, a nematic elastomer (NE) subjected to uniaxial extension deforms without (or with minimal) additional stress up to a certain stretch (*8*–*11*). Ideally, the coupling between the nematic order and elasticity implies that the elastomer deforms spontaneously (i.e., in the absence of stress) when the director rotates in the material frame. This may be understood as a Goldstone mode because of symmetry breaking at the isotropic to nematic phase transition. Briefly, an NE elongates along the director as it undergoes the isotropic to nematic transition. Therefore, changing the director changes the direction of elongation, manifesting itself as a spontaneous deformation. Consequently, when an NE is subjected to a uniaxial extension perpendicular to the director, it accommodates the imposed extension to the extent it can by rotating the director, resulting in soft elasticity. NEs are categorized into aligned monodomain NEs (MNEs) and macroscopically nonaligned polydomain NEs (PNEs), according to the director field. Soft elasticity is observed in both MNEs (when stretched perpendicular to the director), as explained above, and in PNEs. Uniaxial stretching of PNEs with a randomly disordered director field drives a transition to the monodomain state with the global director aligned with the stretching direction (*12*–*18*). This polydomain-to-monodomain transition (PMT) occurs in a finite range of stretch at a small constant force via the local Goldstone-like soft modes. The soft elasticity in the PMT is more pronounced in PNEs with isotropic genesis (I-PNEs) than those with nematic genesis (N-PNEs): I-PNEs and N-PNEs are obtained by cross-linking the mesogens in the high-temperature isotropic state and the low-temperature polydomain nematic state, respectively (*14*, *16*). The cross-linking in the disordered isotropic state for I-PNEs leads to no inherent memory of the initial director field, which is characterized by the texture composed of randomly aligned local domains with fine and uniform sizes (*14*, *19*). Therefore, the local directors in I-PNEs have the great freedom for local directors to rotate. The extremely soft mechanical response of I-PNEs, which is also referred to as "supersoft elasticity," was explained theoretically (*20*, *21*) and demonstrated by simulations (*22*, *23*). The supersoft elasticity effect in I-PNEs was also observed as a large electromechanical effect (*24*).

Previous experimental studies have used uniaxial stretching for the characterization of the nonlinear elasticity of LCEs. Uniaxial stretching, however, is only a particular one among all admissible deformations of elastomers. General biaxial strain, in which the two orthogonal strains are varied independently, covers the whole range of accessible homogeneous deformation of incompressible, isotropic materials such as elastomers (*2*). The general biaxial stress-strain data provide a definite basis for a full understanding of the large deformation behavior of elastomeric materials (*25*). Using general biaxial stretching experiments, the present study reveals a new and unusual in-plane liquid-like mechanical behavior in I-PNEs: The true stresses in the two directions are equal even if the imposed

[1]Department of Macromolecular Science and Engineering, Kyoto Institute of Technology, Sakyo-ku, Kyoto 606-8585, Japan. [2]Department of Mechanical and Civil Engineering, California Institute of Technology, Pasadena, CA 91125, USA. [3]Institute for Materials Chemistry and Engineering, Kyushu University, Nishi-ku, Fukuoka 819-0395, Japan.
*Corresponding author. Email: bhatta@caltech.edu (K.B.); urayama@kit.ac.jp (K.U.)
†These authors contributed equally to this work.

strains in the two directions are unequal. In addition, the true stresses are dictated only by the area variation in the loading plane. We explain that this observed in-plane liquid-like behavior is a generalization of the soft elasticity observed in uniaxial extension or the uniaxial soft elasticity may be understood as a particular manifestation of the in-plane liquid-like behavior.

The wide-angle x-ray scattering (WAXS) measurements characterize the director field in the biaxially stretched I-PNEs. We explain this unique in-plane liquid-like mechanical behavior by theory and full-field three-dimensional (3D) simulations. We foresee that the findings will extend further the potential applications of LCEs.

RESULTS AND DISCUSSION

When conventional elastomers are uniaxially stretched, the tensile stress increases with imposed strain. In LCEs, moderate stretching requires a very low and constant stress that is accompanied by the director rotation (*4*). Figure 1A shows the uniaxial stress (t_x)–stretch (λ_x) curve for an isotropic-genesis main-chain–type PNE (I-MCPNE) with randomly disordered texture. Two types of stress, i.e., true stress (t) and nominal stress (σ) (force per cross section in the deformed and undeformed states, respectively), are used in the figure. The I-MCPNE was fabricated using a thiol-acrylate Michael addition reaction between diacrylate mesogen, di-thiol chain extender, and tetra-thiol cross-linker (Fig. 1B; see Materials and Methods) (*26*). The cross section in the deformed state is estimated assuming volume conservation ($\lambda_x\lambda_y\lambda_z = 1$) during deformation, which is confirmed by a separate experiment (fig. S1), resulting in $t_x = \sigma_x/(\lambda_y\lambda_z) = \sigma_x\lambda_x$. The I-MCPNE before stretching is opaque because of the strong light scattering of disordered birefringent domains. Stretching drives the transition from polydomain to monodomain alignment along the stretching axis, and the monodomain alignment is readily confirmed by a fully transparent appearance. The process of the PMT is characterized by a plateau stress with very low magnitude over a finite range of strain, which has been observed for many types of NEs (*12*–*18*). For the present specimen, PMT ends at $\lambda_x \approx 2$, and the stress monotonically increases with λ_x in the monodomain regime ($\lambda_x > 2$). Similar types of stress-strain behavior are also observed for the MNEs when stretched normally to the initial global director (*4*, *27*–*34*). In NEs, the deformation accompanied by director rotation requires extremely small mechanical work because of the coupling of LC alignment and macroscopic shape (or deformation). This unique mechanical property of NEs has been explained by the concept of (ideal) soft elasticity, which allows the elastomers to deform with no mechanical work by director rotation (*4*, *9*–*11*). Small but nonzero mechanical work observed in real NEs has been interpreted by introducing some non-ideality and viscosity to the original soft elasticity theory (*20*, *21*, *23*, *35*–*37*).

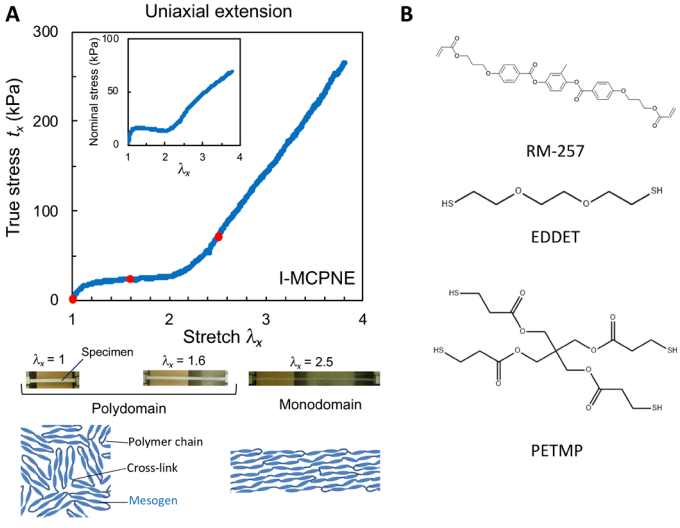

Fig. 1. Uniaxial extension of I-MCPNE. (**A**) Uniaxial extension drives PMT with a small constant stress of about 20 kPa. The initial polydomain is characterized by the turbid appearance reflecting the randomly disordered birefringent domains. The monodomain texture is characterized by the transparent appearance. (**B**) Chemical structures of the compounds.

Biaxial stretching reveals new aspects of soft elasticity in NEs. Figure 2 (A and B) displays the stress-stretch (λ_x) relations in planar extension (PE) for a conventional rubber [styrene-butadiene rubber (SBR)] and I-MCPNE. In PE, the elastomers are stretched in the x direction while keeping the dimension in the y direction unchanged (i.e., $\lambda_y = 1$). As expected quite naturally, in conventional elastomers, the true and nominal stress along the stretching (x) axis is always larger than that along the constraint (y) axis (Fig. 2A). I-MCPNE shows peculiar behavior (Fig. 2B): Nominal stress (σ), which is simply proportional to tensile force, in the constraint (y) direction exceeds that in the stretching (x) direction at $\lambda_x \approx 1.3$. As λ_x increases further, σ_y becomes considerably higher than σ_x. The essence of this unusual behavior becomes evident in true stress (t): Although t_x is always larger than t_y in conventional elastomers, t_x and t_y in I-MCPNE are equal until λ_x reaches about 2.5. In the corresponding strain regime, the specimen has a polydomain texture characterized by the turbid appearance. At further stretching at $\lambda_x > 2.5$, t_x becomes higher than t_y, and the difference becomes larger as λ_x increases. The specimen at $\lambda_x > 2.5$ is considerably transparent, indicating the monodomain alignment along the x axis.

Figure 3 (A and B) shows the results in other types of unequal biaxial (UB) stretching with a nominal strain ratio [$\varepsilon_x/\varepsilon_y$; $\varepsilon_x/\varepsilon_y = (\lambda_x - 1)/(\lambda_y - 1)$] of (5/1) and (5/2), respectively. In these biaxial stretching, the feature $t_x = t_y$ in the polydomain regime is also observed. A similar feature is also confirmed for $\varepsilon_x/\varepsilon_y$ = (5/3) (fig. S2A). For the stretching of $\varepsilon_x/\varepsilon_y$ = 5/1, the PMT completes at $\lambda_x \approx 2.8$, and the inequality $t_x > t_y$ in the monodomain regime appears at $\lambda_x > 2.8$. The end of the PMT is not confirmed for $\varepsilon_x/\varepsilon_y$ = 5/2 and 5/3, and it will require further stretch exceeding the maximum stretch in the figures. The preliminary experiments, however, observed that further stretching resulted in the fracture of the specimen. In equibiaxial (EB) extension, the stresses in the two directions are equal in the whole range of strain (fig. S2B), ensuring no inherent mechanical anisotropy in I-MCPNE. The results in Figs. 2 and 3 indicate that the stretch λ_x required for PMT increases with decreasing the ratio $\varepsilon_x/\varepsilon_y$. This signifies that the constraint in the y direction hinders the director realignment along the larger stretching (x) axis.

The relation $t_x = t_y$ in the polydomain regime is independent of the history of the imposed biaxial strain. This is confirmed by the two-step sequential PE (TPE; Fig. 3C): First, the specimen is stretched along the x axis to $\lambda_x = 1.4$, and second, it is stretched along the y axis to $\lambda_y = 1.8$ from $\lambda_y = 1$ with keeping $\lambda_x = 1.4$. The relation $t_x = t_y$ is observed throughout the deformation process, even when the regime of $\lambda_x > \lambda_y$ shifts to that of $\lambda_y > \lambda_x$.

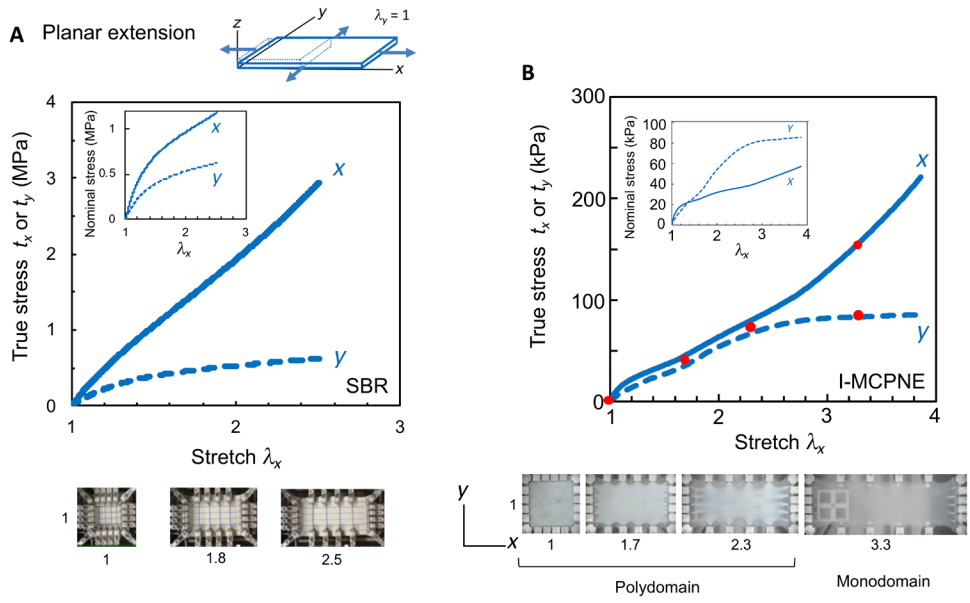

Fig. 2. PE of a conventional elastomer and I-MCPNE. (**A**) When stretched in the *x* direction with keeping the dimension in the *y* direction (PE), conventional elastomers such as SBR always exhibit a larger stress along the stretching (*x*) axis than that along the constraint (*y*) axis. (**B**) I-MCPNE shows the peculiar behavior in PE. Nominal stress in the *y* direction becomes larger than that in the *x* direction at $\lambda_x > 1.3$. Characteristically, the true stresses in the two directions are equal ($t_x \approx t_y$) until the end of PMT ($\lambda_x \approx 2.5$) despite the inequality of $\lambda_x > \lambda_y$. In the monodomain regime ($\lambda_x > 2.5$), t_x becomes larger than t_y as in the case of conventional elastomers.

As can be seen in the photographs of deformed LCEs (Figs. 2 and 3), the portions near the clamps tend to be transparent while the main (middle) part remains turbid, indicating that the strain field is not uniform in the whole area. The detected force is mainly governed by the area subjected to the uniform strain field because the area around the clamps is considerably smaller. It was confirmed for conventional elastomers and gels that the effect around the clamps was negligibly small in the present biaxial tester using sufficiently large specimens (*38*).

The crosshead speed in uniaxial extension (U), EB, PE, and TPE was 0.5 mm/s (corresponding to an initial strain rate of 7.7×10^{-3} s^{-1}). In UB, the crosshead speed in the *x* direction was 0.5 mm/s, whereas that in the *y* direction was 0.1, 0.2, or 0.3 mm/s for a strain ratio of 5/1, 5/2, or 5/3, respectively. The strain rate has a considerable effect on stress in I-MCPNE due to viscoelasticity. Figure S3 shows the stress-stretch relationships in PE at various values of crosshead speed (v). Even at relatively high crosshead speeds ($v = 5$ mm/s), the specimen exhibit the unusual characteristic, i.e., σ_y in the constraint direction considerably exceeds σ_x in the stretching direction at $\lambda_x > 1.5$. The most characteristic feature, i.e., the equality of $t_x \approx t_y$ in the polydomain regime ($\lambda_x < 2.5$), is observed at sufficiently slow crosshead speeds at $v < 0.5$ mm/s, and the magnitude of the stresses still decreases with a reduction in v. The true equilibration requires even slower but practically inaccessible crosshead speed of the order of 0.001 mm/s (*18*). The data at $v = 0.5$ and 0.1 mm/s capture the essential feature of interest, although the stress still includes finite time effect. For the comparison with the theoretical predictions, we used the data at $v_x = 0.5$ mm/s for all types of biaxial stretching because the minimum crosshead $v_y = 0.1$ mm/s in the instrument was used in the *y* direction for UB with a strain ratio of 5/1. The inequality of $t_x > t_y$ at high crosshead speeds ($v = 5$ mm/s) suggests that the specimen does not have enough time to attain the equilibrium polydomain texture during stretching. The dynamics of the texture evolution and stress relaxation under biaxial loading is intriguing, but it is beyond the scope of the present work.

A further prominent characteristic in the polydomain regime is revealed by plotting t_x and t_y against the stretch in the stress-free direction (λ_z) using the data in various types of stretching (Figs. 2B and 3, A and B, and fig. S2A) including EB stretching (fig. S2B). In conventional elastomers (Fig. 4A), the t_x-λ_z and t_y-λ_z curves depend on the type of biaxial stretching because t_x and t_y are a function of both λ_x and λ_y, not a function of only λ_z. In I-MCPNE (Fig. 4B), the t_x-λ_z and t_y-λ_z curves in all types of biaxial stretching in the polydomain regime collapse into a single curve. Parts of individual load curves that deviate from the master curve correspond to the data in the monodomain regime. The master curve obviously indicates the unique feature that t_x (= t_y) is a function of only λ_z, independent of λ_x and λ_y. Since the I-MCPNE is incompressible (fig. S1), $\lambda_x \lambda_y \lambda_z = 1$ or $\lambda_z = 1/\lambda_x\lambda_y$, so that λ_z is inversely proportional to the change of area $\lambda_x\lambda_y$ in the loading plane. Thus, equivalently, the true stress only depends on the change of area (fig. S4 B). This result means that the PNEs can vary their shape freely with no extra mechanical energy when subjected to deformation in the plane: They behave like a liquid in the plane, but like a solid out of the plane. This can be proved by the following argument. The mechanical work required for changing λ_x and λ_y (W) in incompressible elastomers under the condition of the constant area of the loading plane ($\lambda_x \, d\lambda_y + \lambda_y \, d\lambda_x = 0$) is given by

$$\begin{aligned} W &= \sigma_x d\lambda_x + \sigma_y d\lambda_y \\ &= (t_x - t_y)\lambda_y \lambda_z d\lambda_x \end{aligned} \quad (1)$$

Evidently, the equality of true stress ($t_x = t_y$) results in $W = 0$.

The mechanism for the liquid-like behavior where the true stresses in the two orthogonal directions are equalized in any type of biaxial strain is revealed by the 2D WAXS patterns shown in Fig. 5A. The patterns with a diffuse peak arising from intermesogen

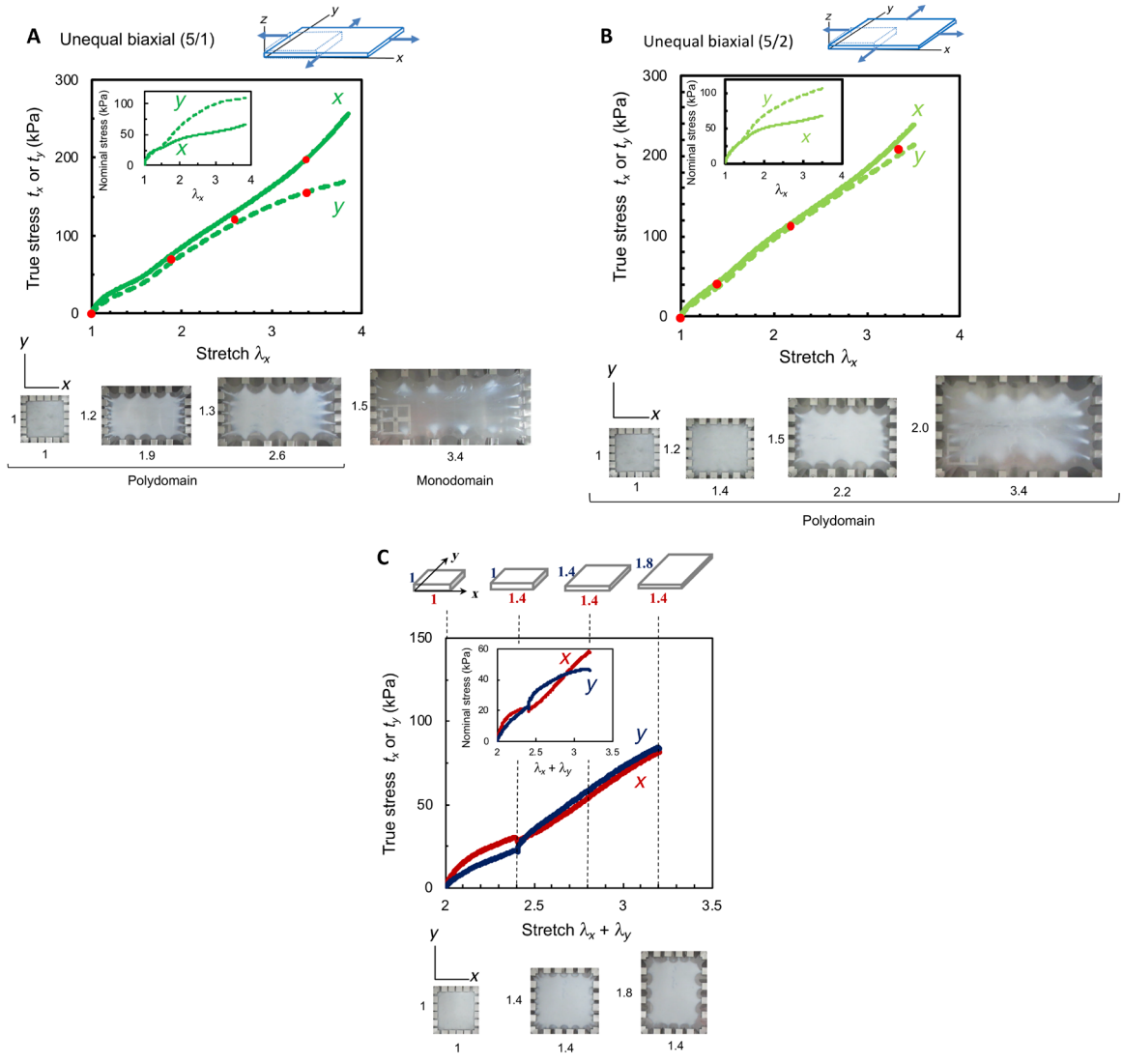

Fig. 3. Equalization of the true stresses in the two directions for various types of biaxial extension of I-MCPNE. (**A** to **C**) True stresses in the two directions are equal in the polydomain regime for the UB stretching with a nominal strain ratio ($\varepsilon_x/\varepsilon_y$) of (5/1) (A) or (5/2) (B) and for the TPE (C). In (A), t_x becomes larger at $\lambda_x > 2.8$ in the monodomain regime. In (B) and (C), the specimens remain polydomain (turbid) in the entire strain range examined, since the transition to the monodomain requires the stretch exceeding the accessible strain in the experiments. In (C), the equality $t_x \approx t_y$ continues throughout the stretching process, despite the shift of the regime of $\lambda_x > \lambda_y$ to that of $\lambda_y > \lambda_x$. The corresponding results of the biaxial stretching with a value of $\varepsilon_x/\varepsilon_y$ of (1/1) or (5/3) are shown in figs. S2 and S3, respectively.

distance (about 0.43 nm) are typical for nematic LCs (*39*), and the isotropic pattern in the undeformed state reflects the randomly disordered polydomain alignment. In EB stretching, the pattern remains almost isotropic regardless of strain, exhibiting that the local nematic director stays nearly random in the *x*-*y* plane. In UB stretching including PE, the azimuthal redistribution of intensity of the pronounced scattering ring proceeds with stretching (an increase in λ_x), indicating an increase in the mean orientational order parameter (S_m) of the local nematic director in the larger strain (*x*) direction. When compared at the same λ_z, S_m becomes higher as the anisotropy of biaxial strain field (characterized by $\varepsilon_x/\varepsilon_y$) becomes larger (Fig. 5B): S_m (PE) > S_m [UB(5/1)] > S_m [UB(5/2)] > S_m (EB). Furthermore, we expect $S_m = 2Q/3$ for uniform distribution and $S_m = Q/6$ for planar EB orientation, where Q is the microscopic orientation order parameter (see Materials and Methods). Our observations for $S_m = 0.4$ for the monodomain in U are consistent with $Q = 0.6$, which is in the expected range for LCEs (*4*).

The distributions show symmetry about the horizontal loading axis, indicating that the directors arrange themselves on average to cancel any shear. Thus, the director distribution follows imposed strain to relieve the difference between the true stress. This suggests that liquid-like behavior emerges at the mesoscale, whereas it remains a solid at small scales (Fig. 6). The equal true stress dictated by only λ_z is independent of the director field (S_m). Note that the biaxial strain fields in tensile and WAXS measurements with the same values of λ_x and λ_y will not be exactly identical because of the difference in the clamping and stretching mechanism (see Materials and Methods). The difference, however, does not affect the essential feature revealed here, i.e., the independency of the equal true stress on S_m.

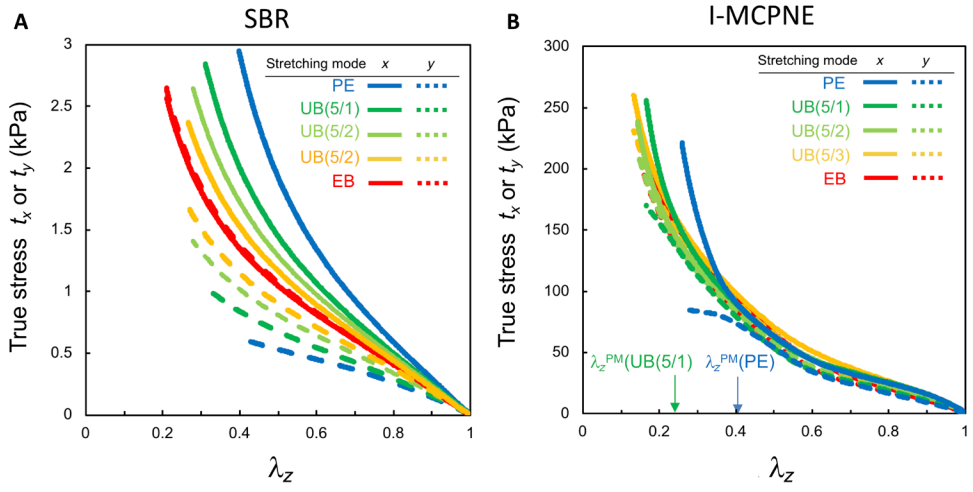

Fig. 4. Biaxial true stresses as a function of dimensional change in the stress-free (*z*) direction in various types of biaxial strain for I-MCPNE. (**A**) In conventional elastomers, t_x-λ_z and t_y-λ_z relations depend on the type of biaxial stretching. (**B**) In I-MCPNE, t_x-λ_z and t_y-λ_z relations in all types of biaxial stretching collapse into a single master curve. Parts of individual load curves that deviate from the master curve correspond to the data in the monodomain regime. The master curve indicates that t_x (= t_y) in the polydomain regime is dictated by only λ_z (or the area variation $\lambda_x\lambda_y$), independently of λ_x and λ_y.

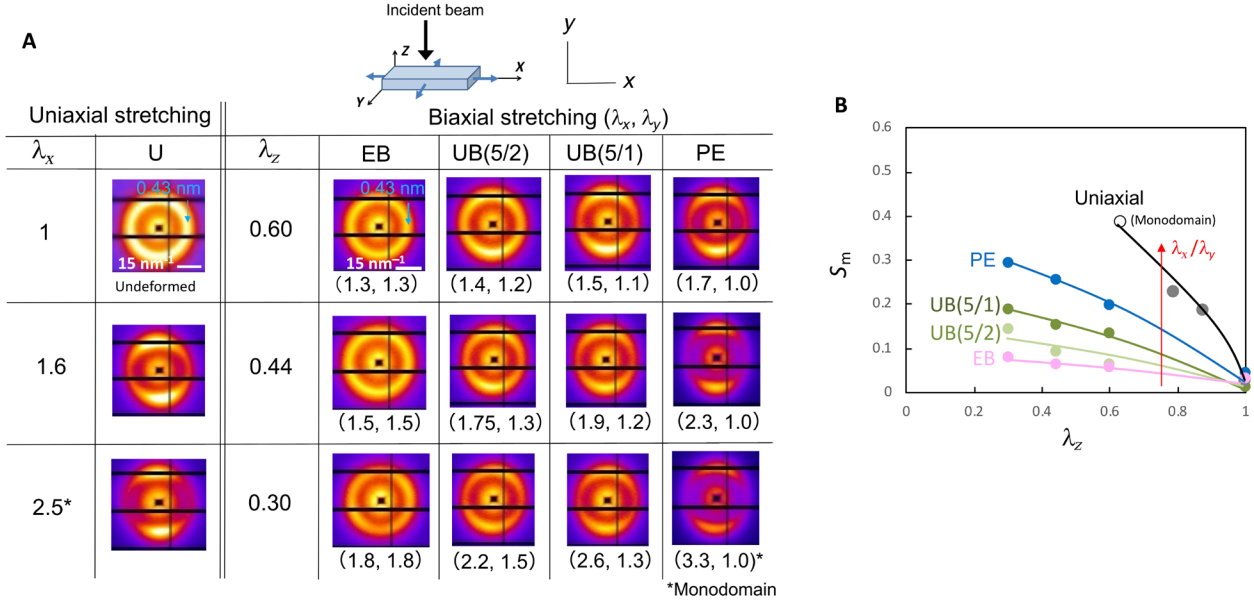

Fig. 5. 2D WAXS patterns in various types of biaxial strain for I-MCPNE. (**A** and **B**) Mean orientational order (S_m) of the local nematic director in the larger strain (*x*) direction increases with an increase in λ_x in unequal stretching (UB) including PE. When compared at the same λ_z, S_m becomes higher as the anisotropy of biaxial strain field ($\varepsilon_x/\varepsilon_y$) becomes larger.

We comment that the liquid-like behavior reported here is a generalization of the classical super-soft behavior observed in uniaxial extension (*8*). The reorientation and alignment of the LC domains accommodate shear (no change of area) and thus lead to an equalization of the two principal stresses ($t_x \approx t_y$). In the uniaxial extension (U), lateral edges are free, and thus, one principal stress is necessarily zero ($t_y = 0$). It follows then that the axial stress is also almost zero, and this is the classical super-soft behavior. In other words, the classical super-soft behavior is a manifestation of the liquid-like behavior. There is, however, an interesting difference in the way it manifests itself in the t_x versus λ_x curve: There is a plateau in U (Fig. 1A) but no noticeable plateau in biaxial stretch (e.g. PE; Fig. 2B). In U, $t_x \approx t_y \approx 0$ as explained above gives rise to the plateau. In contrast, in biaxial deformation (PE, UB, and EB), the lateral edge is not free, and thus, $t_y \neq 0$, which implies that $t_x \neq 0$, and there is no plateau. However, we have the same in-plane liquid-like behavior ($t_x \approx t_y$) in all situations. It just manifests itself in a special manner in uniaxial stretch because the lateral edge happens to be free.

These observations and the mechanisms responsible are further examined from theoretical considerations. The isotropic-genesis NEs has three contributions to the free energy (*20*, *21*)—the entropic

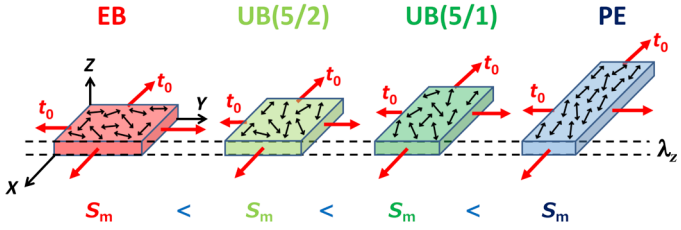

Fig. 6. The equal true stress is only dependent on the thickness change (or the area change in the loading plane), independent of the director field (S_m). PNEs can vary their shape freely with no extra mechanical energy when subjected to deformation in plane, behaving like liquid in the plane but like solid out of the plane.

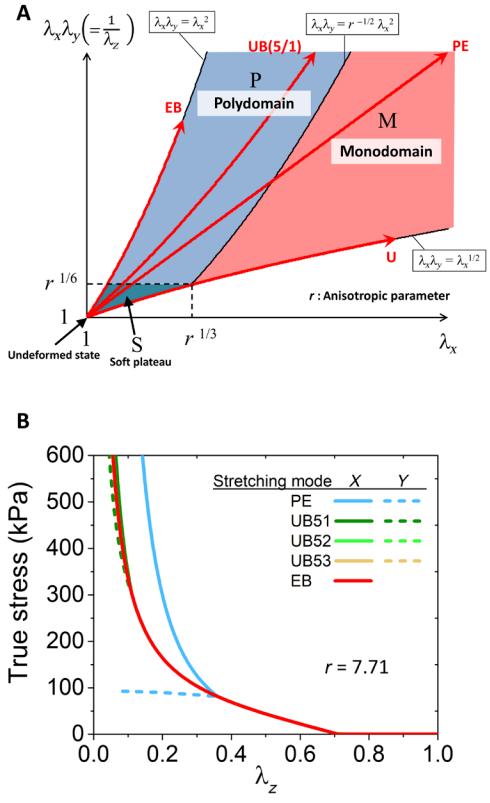

Fig. 7. State diagram and true stress–λ_z relations of isotropic-genesis NEs by a theory with ideal approximation. (**A**) The three regimes are classified as the functions of λ_x (larger stretch) and $\lambda_x\lambda_y$ (area variation in the loading plane) or λ_z (thickness variation): 3D distributed directors exhibiting soft behavior with zero stress (S regime); the directors fully aligned along the *x* axis (M regime); planar (but nonuniform) distribution of directors with a reflection symmetry about the *x* axis (P regime). The red arrows indicate the loading paths. (**B**) In the P regime, the directors can realign in the plane, thereby the true stresses are equalized and governed by only $\lambda_x\lambda_y$ or equivalently by only λ_z. The zero-stress region corresponds to the S regime, and the branches correspond to the data in the M regime. The *r* value ($r = 7.71$) is evaluated from the plateau width (λ_p) in U ($\lambda_p = r^{1/3}$).

elasticity of the Gaussian polymer chains, the non-ideality reflecting the disorder in the material, and the Frank elasticity (see Materials and Methods). In the ideal approximation ($\alpha, \kappa \to 0$), the behavior and the stress have been explicitly characterized in prior work (detailed expressions in Materials and Methods) (*40*). There are three regimes as shown in Fig. 7A where *r* is a characteristic parameter for the anisotropy of the configuration of network strands. The anisotropy parameter *r* is related to the microscopic orientation order parameter *Q* and the nature of the polymer chain. It is possible to show that $Q = (r - 1)/(r + 2)$ for a freely jointed rod model (*10*), although the exact relation for a more realistic polymer chain is not known. In PNEs, the parameter *r* also determines the uniaxial stretch required for PMT (λ_p), that is, the end of the plateau in the t_x versus λ_x curve in U (Fig. 1A), as $\lambda_p = r^{1/3}$ (*8*). In the first regime (labeled S), the directors are distributed in 3D and can realign to attain soft behavior with zero stress. The directors become planar in the second regime labeled P; the directors are still not uniform but are planar and display a reflection symmetry about the *x* axis. They can realign in the plane, and therefore, the true stresses are equal and only a function of $\lambda_x\lambda_y$ or, equivalently, only a function of λ_z (Fig. 7B). The directors are fully aligned in the third region labeled M. The loading paths are also shown in Fig. 7A. The uniaxial stress (U) initially in S displays soft behavior and then goes to M. The PE goes from S to P to M displaying soft behavior, equal true stress and, lastly, unequal true stress. Last, the EB shows soft and then equal true stress. This diagram also explains the effects of the type of biaxial strain on the threshold of PMT (the boundary between P and M) observed in the experiments. The stretch λ_x required for PMT increases with increasing λ_y. All this complex behavior is described by only two parameters—modulus *G* and anisotropy *r*.

Still, this ideal approximation does not have a length scale, and it does not describe either the finite stress plateau in U or the details of the director distribution. Figure 8 displays the results of full-field 3D simulations with the free energy (including non-ideality and Frank elasticity) and a time-dependent evolution for the director (see Materials and Methods). The model has five parameters that are fitted to U and PE and held fixed for the remaining simulations. Figure 8 (A to C) shows the true stress-stretch behavior for U, PE, and UB(5/1) and compares them with experimental observations [see fig. S5 for UB(5/2), UB(5/3), and EB]. The true stresses in the polydomain regime are indeed equal in PE, UB, and EB until the end of PMT and depend only on λ_z (Fig. 8D). The model accurately describes the behavior over these various protocols with a single set of only four parameters. Figure 8 (A to C) and figs. S5 and S6 also show the director distribution in real space (the color represents the angle of the planar component of the director) and the computed distribution. The evolution of the mean orientational order parameter S_m and the biaxial order parameter *X* (precise definition in Materials and Methods) is shown in Fig. 8E. The animations of these simulations are provided in the Supplementary Materials. Each simulation begins with the same equidistributed director distribution. In U, the directors simultaneously align into the plane (*X*) and in the plane (S_m) toward the loading direction as intuitively expected. In PE and UB, the directors orient simultaneously into the plane and in the plane, but the evolution into the plane is faster and complete before the full orientation in the plane. In EB, there is orientation into the plane but no reorientation in the plane. The full-field images show no discernable order like stripe domains. Still, director angular distributions show symmetry about the horizontal loading axis as in the experiments. Last, fitting the stress versus stretch data provides an anisotropy parameter of $r = 7.71$ (see Materials and Methods), which, in turn, yields the value $Q = 0.69$ using the relation $Q = (r - 1)/(r + 2) = 0.69$, which was derived for the

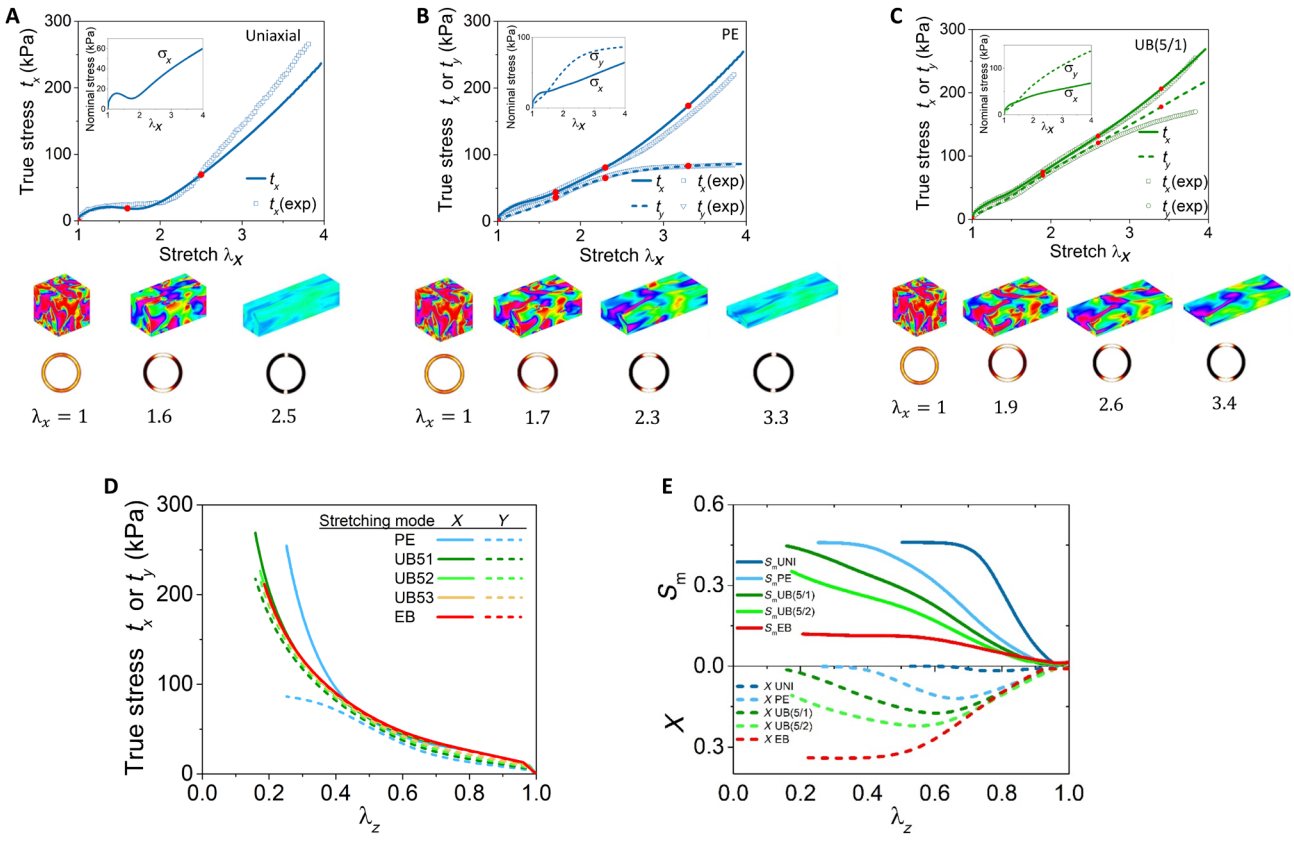

Fig. 8. Theoretical true stress–stretch relations and director distribution for various types of extension obtained by the full-field 3D simulations with the free energy including nonideal and Frank elasticity and a time-dependent evolution for the director. The theoretical true stress–stretch relations satisfactorily describe the experimental ones in uniaxial (**A**), planar (**B**), and UB stretching with a strain ratio ($\varepsilon_x/\varepsilon_y$) = (5/1) (**C**). The insets show the nominal stress–stretch relations. The director field in real space and the corresponding diffraction patterns are also displayed. The color represents the angle of the planar component of the director. The corresponding data for the biaxial stretching of a ratio $\varepsilon_x/\varepsilon_y$ of (5/2), (5/3), and (1/1) are available in fig. S5. (**D**) The true stresses in the polydomain regime are indeed equal for all types of biaxial stretching and dictated only by thickness change (λ_z), in agreement with the experimental results (Fig. 3B). The branches correspond to the data in the monodomain regime. (**E**) The evolutions of the planar mean orientational order parameter (S_m) and the mean biaxial orientational order parameter (X) are also obtained as a function of λ_z in each type of stretching. The calculations (A to E) in all types of biaxial stretching are made using the same parameter set.

freely jointed rod model (*10*). This compares very well with the experimental value $Q = 0.6$ ($S_m = 0.4$) obtained in Fig. 5B, considering the fact that the freely jointed rod model is better suited for the side-chain polymers (*4*) instead of the main-chain polymers used here. All of these establish that the balancing of the true stress and the consequently in-plane liquid-like behavior occurs at the mesoscale despite the disorder and the non-ideality in the system.

In summary, we reveal the in-plane liquid-like behavior of I-MCPNE: The orthogonal true stresses are equalized in any type of biaxial strain, dictated only by the area variation in the loading plane and equivalently only by the dimensional change in the stress-free direction, as long as it remains in a polydomain state. The in-plane liquid-like behavior is successfully explained by the full-field 3D simulations. It would be very interesting to see in future work whether the in-plane liquid-like behavior observed here is seen in the LCEs with different chemical structures. The unparalleled mechanical behavior of I-MCPNE enables manifold applications including wrinkle-free membranes and adaptable materials. Eliminating wrinkles in membranes has been a long-standing problem because wrinkling severely degrades their performances in deployable antenna, solar sails and shields, and morphing wing applications. Conventional thin membranes are inevitably susceptible to nonuniform in-plane deformation resulting in wrinkling because of their poor resistance to shear, and thus, they require the extra complex mechanisms to rebalance the tension, which changes with temperature and other environmental conditions (*41*). The I-MCPNE–based membranes provide a means to avoid the problem because they can accommodate shear without any shear stress and balance the tension automatically (see Supplementary Text). Similar instabilities arise when flat membranes are wrapped or draped over uneven or complex-shaped objects as required in medicine, packaging, and clothing. Such draping changes the Gauss curvature, and this, in turn, may induce shear. The ability of I-MCPNE to undergo a range of shear without any shear stress avoids instabilities associated with draping of complex and changing surfaces. I-MCPNE exhibits apparent plastic deformation due to hysteresis, but the true stresses in the two directions will remain equal even during unloading. Since wrinkling is driven by unequal true stresses, we expect it to be suppressed even during unloading. Last, the peculiar mechanical behavior of I-MCPNE is a result of mesoscale rather than molecular scale, providing insights into the design of artificial metamaterials with the similar in-plane liquid-like features.

MATERIALS AND METHODS

Sample preparation

The I-MCPNE membrane was fabricated using a thiol-acrylate Michael addition reaction (*26*, *42*). The diacrylate mesogen, 1,4-bis[4-(3-acryloyloxyproopoxy)benzoyloxy]-2-methylbenzene (RM-257), was purchased from Tokyo Chemical Industries (Tokyo, Japan). Two thiol monomers, 2,2′-(ethylenedioxyl) diethanethiol (EDDET) and pentaerythritol tetrakis (3-mercaptopropionate) (PETMP), were purchased from Sigma-Aldrich (St. Louis, MO, USA). Figure 1B shows the chemical structure of each compound. RM-257 was dissolved in toluene at 80°C, and then EDDET and PETMP were added to the solution so that the concentration of the total compounds could be 70 weight % (wt %). The molar ratio of RM-257/EDDET/PETMP is 1/0.74/0.06. The catalyst dipropyl amine (DPA) was purchased from Sigma-Aldrich. The DPA was first diluted in toluene at a weight ratio of 1/47. The DPA solution was added to the mixture solution at a molar ratio of RM-257/DPA = 1/0.017 and mixed vigorously to ensure a homogeneous mixture.

The solution was poured into a mold and left to undergo the thiol-acrylate reaction at 25°C where the mixture is in the isotropic state for 12 hours. The resultant free-standing gel film was transparent, ensuring the cross-linking in the isotropic state (i.e., isotropic genesis). The gel film was further left in air at 25°C for 3 days. The opaque I-MCPNE film was obtained by drying the film completely under a reduced pressure of 70 kPa at 80°C for 90 min.

SBR (styrene content: 25%, TUFDENE 2000, Asahi Kasei Corp.) with a small volume fraction (5%) of silica (Nipsil, Tosoh Silica Corporation) was used for comparison. Bis(triethoxysilylpropyl)polysulfide (Shin-Etsu Chemical Co.) was used as a silane-coupling agent, forming covalent bonds between the silica filler surface and the rubber matrix. The specimen was made using a Brabender mixer at a mixing speed of 80 rounds/min at 110°C. The concentration of sulfur for cross-linking was 1.4 wt %.

Biaxial and uniaxial tensile tests

Biaxial tensile tests of I-MCPNE and SBR were conducted at 25°C with a custom-made tester BIS-0707 or ISBT-2306 (IS Giken, Kyoto, Japan), respectively. Each of the biaxial testers is optimized for the measurements of considerably soft gels or rigid elastomers. The details of each tester were described elsewhere (*38*, *43*). The two tensile forces in the orthogonal directions (f_x and f_y, respectively) were measured as the functions of the stretch ratios in the x and y directions (λ_x and λ_y, respectively): $\lambda_i = l_i/l_0$ where l_i and l_0 are the dimensions in the deformed and undeformed states in the i direction ($i = x,y$). Six types of biaxial stretching were used (fig. S7): Equiaxial extension with $\lambda_x = \lambda_y$ (EB), PE that holds the dimension in the y direction unchanged ($\lambda_y = 1$), UB extension with a constant strain ratio (UB) [$(\lambda_x - 1)/(\lambda_y - 1) = \varepsilon_x/\varepsilon_y$ = 5/1, 5/2, 5/3]. In the TPE, the specimen was first stretched to λ_x = 1.4 with λ_y = 1 and then stretched in the y direction with keeping λ_x = 1.4. In EB, PE, and TPE, the crosshead speed was 0.5 mm/s. In UB with $\varepsilon_x/\varepsilon_y$ = 5/1, 5/2, 5/3, the crosshead speed in the x direction was 0.5 mm/s while that in the y direction was 0.1, 0.2, or 0.3 mm/s, respectively. The stress is substantially dependent on the strain rate due to the pronounced viscoelasticity (fig. S3), and the true equilibration requires extremely slow but practically inaccessible crosshead speed (<0.01 mm/s). The data at v = 0.5 mm/s, however, exhibit the key feature of interest (i.e., $t_x \approx t_y$), although the stress is not equilibrated. The detailed discussion is also given in the Results and discussion.

The I-MCPNE or SBR specimens with dimensions of 65 mm by 65 mm and a thickness of 0.7 or 2 mm, respectively, were used for the biaxial stretching measurements. The effects of the complicated deformation around the chucks on the detected force will likely be small as the corresponding area is small relative to the area subjected to the uniform strain field. It was confirmed for conventional elastomers and gels that the corresponding effect is negligibly small in the present custom-made biaxial testers (*38*, *43*). These biaxial testers require the relatively large specimens (65 mm by 65 mm), and this requirement is for satisfying the condition in which the detected force is governed by the area subjected to the uniform strain field.

Uniaxial tensile tests were conducted at 25°C with an AC-500N-CM (TSE Co., Yokohama, Japan) for the specimen with dimensions of 65 mm by 6 mm by 0.7 mm. The gauge length and crosshead speed (0.5 mm/s) were the same as in the biaxial tensile tests.

The specimen was not stretched to failure in each deformation, and the same specimen was used in all deformations. The failure point was evaluated in the preliminary experiments. After releasing the imposed strain, the specimen required an extremely long time to recover the initial dimensions. To accelerate the shape recovery, the unloaded specimen was placed for 1 min at 90°C beyond the nematic-isotropic transition point (ca. 80°C) and then cooled to 25°C. The tensile properties were repeatable for the specimens subjected to multiple heating/cooling cycles (fig. S8).

Wide-angle x-ray diffraction measurement

In situ WAX diffraction measurement was carried out during various deformation modes (PE, UB, and PE) at BL05XU at SPring-8 using a homemade biaxial tester (JUNKEN MEDICAL Co. Ltd.), which is specially designed for the x-ray beamline (fig. S9). PILATUS 1M (DECTRIS Ltd.; pixel size, 172 μm^2) was used as a detector. Camera length, beam size, wavelength of x-ray, and exposure time were 100 mm, 200 μm^2, 0.1 nm, and 1 s, respectively. The measurements of the LCE film specimen (10 mm by 10 mm by 0.7 mm) under biaxial strain were conducted at the same strain rate (8×10^{-3} s^{-1}) as in the mechanical tensile tests for four types of biaxial stretching: EB stretching, UB stretching with $\varepsilon_x/\varepsilon_y$ = 5/1 and 5/2, and PE. The 2D diffraction patterns were obtained at 25 positions at intervals of 0.5 mm in the central area of the stretched specimens (2.5 mm by 2.5 mm) (fig. S10). Obtained 2D patterns were reduced to 1D profiles by integrating with a software, FIT2D (version 12.077, A. Hammersley) (fig. S11). Mean orientational order (S_m) was calculated using Hermans' method (*44*) at q = 14.2 to 14.8 nm^{-1}. The values of S_m in Fig. 5B are the average of the data at 25 positions.

Theoretical approach

The free energy of an isotropic-genesis NE may be described as (*20*, *21*)

$$E[y,n] = \int_V W(F,n,\nabla n;n_0)\,dV$$
$$= \int_V \left(\frac{G}{2}(\mathrm{tr}\,F^T \ell^{-1} F - 3) + \frac{\alpha}{2}(|F^T n|^2 - (n_0 \cdot F^T n)^2) + \frac{\kappa}{2}|\nabla n|^2 \right) dV \quad (2)$$

where $F = \nabla y$ is the deformation gradient, n is the director orientation, $\ell = r^{-1/3}(I - (r-1)nn)$ is the step-length tensor depending on the anisotropy parameter $r > 1$, and $n_0(x)$ is a random unit vector field. The first term is the Gaussian elasticity of the elastomer with

shear modulus G (*4*, *10*); the second, depending on a parameter $\alpha > 0$, describes the random disorder of the network (*45*), which leads to a preferred random director field $n_0(x)$; and the final is the Frank elasticity that penalizes changes of director orientation in the single constant approximation. Similar free energy formulations have been used in the literature (*21*) with a slightly different formulation for the term describing randomness. We may view this as a finite deformation generalization of a Landau-Ginzburg–type free energy where the first term describes the energy landscape of the order parameters, the second term the role of the disorder, and the third term the exchange energy.

Experimentally, $\alpha/G \sim 10^{-4}$ and $\sqrt{\kappa/G} \sim 10$ nm, and one can ignore them to leading order. This leads to the ideal model in the approximation $\alpha, \kappa \to 0$. It is possible to obtain exact results for the response of the sheet subjected to biaxial stretching as done in prior work (*40*). These results show various regimes and provide an explicit formula for the stress and characterization of the domains (Table 1).

In the general nonideal setting (i.e., in the absence of the approximation $\alpha, \kappa \to 0$), it is not possible to derive explicit results. So, numerical simulations were performed in 3D to solve the mechanical equilibrium $\delta_F E + \nu_F \dot{F} = 0$ and director evolution $\nu_n \dot{n} = -\delta_n E$. We may view these equations as the finite deformation generalization of time-dependent Landau-Ginzburg theory. We discretize these differential equations implicitly in time using backward Euler discretization, and the resulting equations can be written as a variational problem at the kth time step

$$y^k, n^k = \arg\min \int_V W(\nabla y, n, \nabla n; n_0)\, dV + \frac{\nu_F}{2\Delta t}\int_V |\nabla y - F^{k-1}|^2\, dV + \frac{\nu_n}{2\Delta t}\int_V |n - n^{k-1}|^2\, dV \quad (3)$$

subject to the constraint $\det \nabla y = 1, |n| = 1$ and periodic boundary condition with prescribed λ_x, λ_y, and $\sigma_z = 0$. We discretize this problem on a 128^3 finite difference grid and solve it using a fast Fourier transform–based numerical method introduced by Zhou and Bhattacharya (*46*) (additional details in the Supplementary Materials). It is important that the computational volume V is large compared to the length scale determined by $\sqrt{\kappa/G}$ to ensure macroscopic response while the spatial discretization is smaller than that determined by $\sqrt{\kappa/G}$ to ensure sufficient spatial resolution. We have found that the 128^3 grid meets this criterion.

The preferred director distribution n_0 is obtained as follows: We generate a random distribution (equidistributed on the unit sphere) on our 128^3 grid and filter it by removing Fourier coefficients that are smaller than the length scale determined by $\sqrt{\kappa/G}$ (smaller fluctuations do not have any effect on the results because the model filters them away but adds to the computational cost). We then relax our computational domain under zero stress to obtain our initial specimen. This specimen is typically internally stressed (with zero average) because the preferred director distribution n_0 may not be kinematically compatible. We start all our loading protocols with this specimen. We have verified through select examples that our results are independent of the initial random distribution. These computations are expensive and solved on a computational cluster with a compute node consisting of a 14-core Intel Broadwell CPU and four Nvidia Tesla P100 GPUs. The parameters $G = 23.63$ kPa, $r = 7.71$, $\alpha = 0.06$, $\nu_F = 2.53$ Pa·s, and $\nu_n = 0.01$ Pa·s are obtained by fitting the computed results to the experimental observations of the uniaxial stretch and PE.

To compute the orientation distribution and the order parameter, recall that the orientation distribution tensor in a polydomain specimen is

$$\begin{aligned} S_{ij} &= \langle u_i u_j - 1/3\, \delta_{ij} \rangle_{\text{molecules in the polydomain specimen}} \\ &= \langle \langle u_i u_j - 1/3\, \delta_{ij} \rangle_{\text{molecules in a domain}} \rangle_{\text{domains in the specimen}} \\ &= \langle \langle u_i u_j - 1/3\, \delta_{ij} \rangle_{\text{ensemble at } x} \rangle_x = \langle Q(n_i n_j - 1/3\, \delta_{ij}) \rangle_x \\ &= Q \langle (n_i n_j - 1/3\, \delta_{ij}) \rangle_x \end{aligned}$$

where u_i is the orientation of a nematic mesogen, and Q is the microscopic order parameter. We define the mean orientational order parameter S_m to be the largest eigenvalue of S_{ij} and the biaxial order parameter X to be the difference between the two smallest eigenvalues of S_{ij}. It follows that $S_m = 2Q/3$, $X = 0$ for perfectly aligned domains, $S_m = Q/6$, $X = Q/2$ for equidistributed domains in the plane, and $S_m = 0$, $X = 0$ for equidistributed domains. We use the relation $Q = (r-1)/(r+2)$, which was derived for the freely jointed rod model (*10*).

Table 1. Explicit formula for the distinct regions of stretch and the corresponding state of stress and morphology according to the ideal theory.

Region	Strain range	Stress	Morphology
S	$\lambda_x\lambda_y \le r^{1/6}, \lambda_y \le \lambda_x \le \lambda_y^{-2}$	$t_x = t_y = 0$	3D polydomain
P	$\lambda_x\lambda_y > r^{1/6}$, $r^{-1/2}\lambda_x^2 < \lambda_x\lambda_y \le \lambda_x^2$	$t_x = t_y = Gr^{1/3}\left(\frac{\lambda_x\lambda_y}{r^{1/2}} - \frac{1}{\lambda_x^2\lambda_y^2}\right)$	2D polydomain with reflection symmetry
M	$\lambda_x^{1/2} \le \lambda_x\lambda_y \le r^{-1/2}\lambda_x^2$	$t_x = Gr^{\frac{1}{3}}\left(\frac{\lambda_x^2}{r} - \frac{1}{\lambda_x^2\lambda_y^2}\right)$, $t_y = Gr^{1/3}\left(\frac{\lambda_y^2}{\lambda_x^2} - \frac{1}{\lambda_x^2\lambda_y^2}\right)$	Monodomain

SUPPLEMENTARY MATERIALS

Supplementary material for this article is available at http://advances.sciencemag.org/cgi/content/full/7/25/eabe9495/DC1

REFERENCES AND NOTES

1. P. J. Flory, *Principles of Polymer Chemistry* (Cornell Univ. Press, 1953).
2. L. R. G. Treloar, *The Physics of Rubber Elasticity* (Clarendon Press, 1975).
3. M. Rubinstein, R. H. Colby, *Polymer Physics* (Oxford Univ. Press, 2003).
4. M. Warner, E. M. Terentjev, *Liquid Crystals Elastomers (Revised Edition)* (Clarendon Press, 2007).
5. F. Brömmel, D. Kramer, H. Finkelmann, Preparation of liquid crystal elasotmers. *Adv. Polym. Sci.* **250**, 1–48 (2012).
6. S. W. Ula, N. A. Traugutt, R. H. Volpe, R. R. Patel, K. Yu, C. M. Yakacki, Liquid crystal elastomers: An introduction and review of emerging technologies. *Liq. Cryst. Rev.* **6**, 78–107 (2018).
7. T. J. White, D. J. Broer, Programmable and adaptive mechanics with liquid crystal polymer networks and elastomers. *Nat. Mater.* **14**, 1087–1098 (2015).
8. M. Warner, E. M. Terentjev, *Liquid Crystals Elastomers* (Clarendon Press, 2003).
9. L. Golubovic, T. C. Lubensky, Nonlinear elasticity of amorphous solids. *Phys. Rev. Lett.* **63**, 1082–1085 (1989).
10. P. Bladon, E. M. Terentjev, M. Warner, Transitions and instabilities in liquid crystal elastomers. *Phys. Rev. E.* **47**, R3838–R3840 (1993).

11. S. Conti, A. DeSimone, G. Dolzmann, Soft elastic response of stretched sheets of nematic elastomers: A numerical study. *J. Mech. Phys. Solids* **50**, 1431–1451 (2002).
12. J. Schätzle, W. Kaufhold, H. Finkelmann, Nematic elastomers: The influence of external mechanical stress on the liquid-crystalline phase behavior. *Makromol. Chem.* **190**, 3269–3284 (1989).
13. S. M. Clarke, E. M. Terentjev, I. Kundler, H. Finkelmann, Texture evolution during the polydomain-monodomain transition in nematic elastomers. *Macromolecules* **31**, 4862–4872 (1998).
14. K. Urayama, E. Kohmon, M. Kojima, T. Takigawa, Polydomain–monodomain transition of randomly disordered nematic elastomers with different cross-linking histories. *Macromolecules* **42**, 4084–4089 (2009).
15. A. Azoug, V. Vasconcellos, J. Dooling, M. Saed, C. M. Yakacki, T. D. Nguyen, Viscoelasticity of the polydomain-monodomain transition in main-chain liquid crystal elastomers. *Polymer* **98**, 165–171 (2016).
16. N. A. Traugutt, R. H. Volpe, M. S. Bollinger, M. O. Saed, A. H. Torbati, K. Yu, N. Dadivanyan, C. M. Yakacki, Liquid-crystal order during synthesis affects main-chain liquid-crystal elastomer behavior. *Soft Matter* **13**, 7013–7025 (2017).
17. A. Agrawal, A. C. Chipara, Y. Shamoo, P. K. Patra, B. J. Carey, P. M. Ajayan, W. G. Chapman, R. Verduzco, Dynamic self-stiffening in liquid crystal elastomers. *Nat. Commun.* **4**, 1739 (2013).
18. A. Takebe, K. Urayama, Supersoft elasticity and slow dynamics of isotropic-genesis polydomain liquid crystal elastomers investigated by loading- and strain-rate–controlled tests. *Phys. Rev. E.* **102**, 12701 (2020).
19. H. Higaki, K. Urayama, T. Takigawa, Memory and development of textures of polydomain nematic elastomers. *Macromol. Chem. Phys.* **213**, 1907–1912 (2012).
20. J. S. Biggins, M. Warner, K. Bhattacharya, Supersoft elasticity in polydomain nematic elastomers. *Phys. Rev. Lett.* **103**, 037802 (2009).
21. J. S. Biggins, M. Warner, K. Bhattacharya, Elasticity of polydomain liquid crystal elastomers. *J. Mech. Phys. Solids* **60**, 573–590 (2012).
22. N. Uchida, Soft and nonsoft structural transitions in disordered nematic networks. *Phys. Rev. E.* **62**, 5119–5136 (2000).
23. G. Skaçej, C. Zannoni, Molecular simulations shed light on supersoft elasticity in polydomain liquid crystal elastomers. *Macromolecules* **47**, 8824–8832 (2014).
24. T. Okamoto, K. Urayama, T. Takigawa, Large electromechanical effect of isotropic-genesis polydomain nematic elastomers. *Soft Matter* **7**, 10585–10589 (2011).
25. K. Urayama, New aspects of nonlinear elasticity of polymer gels and elastomers revealed by stretching experiments in various geometries. *Polym. Int.* **66**, 195–206 (2017).
26. C. M. Yakacki, M. Saed, D. P. Nair, T. Gong, S. M. Reed, C. N. Bowman, Tailorable and programmable liquid-crystalline elastomers using a two-stage thiol-acrylate reaction. *RSC Adv.* **5**, 18997–19001 (2015).
27. J. Kupfer, H. Finkelmann, Nematic liquid single-crystal elastomers. *Makromol. Chemie-Rapid Commun.* **12**, 717–726 (1991).
28. S. M. Clarke, A. Hotta, A. R. Tajbakhsh, E. M. Terentjev, Effect of cross-linker geometry on equilibrium thermal and mechanical properties of nematic elastomers. *Phys. Rev. E.* **64**, 61702 (2001).
29. D. L. Thomsen, P. Keller, J. Naciri, R. Pink, H. Jeon, D. Shenoy, B. R. Ratna, Liquid crystal elastomers with mechanical properties of a muscle. *Macromolecules* **34**, 5868–5875 (2001).
30. A. Petelin, M. Čopič, Observation of a soft mode of elastic instability in liquid crystal elastomers. *Phys. Rev. Lett.* **103**, 77801 (2009).
31. K. Urayama, R. Mashita, I. Kobayashi, T. Takigawa, Stretching-induced director rotation in thin films of liquid crystal elastomers with homeotropic alignment. *Macromolecules* **40**, 7665–7670 (2007).
32. N. P. Godman, B. A. Kowalski, A. D. Auguste, H. Koerner, T. J. White, Synthesis of elastomeric liquid crystalline polymer networks via chain transfer. *ACS Macro Lett.* **6**, 1290–1295 (2017).
33. D. Mistry, P. B. Morgan, J. H. Clamp, H. F. Gleeson, New insights into the nature of semi-soft elasticity and "mechanical-Fréedericksz transitions" in liquid crystal elastomers. *Soft Matter* **14**, 1301–1310 (2018).
34. T. H. Ware, J. S. Biggins, A. F. Shick, M. Warner, T. J. White, Localized soft elasticity in liquid crystal elastomers. *Nat. Commun.* **7**, 10781 (2016).
35. G. C. Verwey, M. Warner, E. M. Terentjev, Elastic instability and stripe domains in liquid crystalline elastomers. *J. Phys. Ii.* **6**, 1273–1290 (1996).
36. S. Conti, A. DeSimone, G. Dolzmann, Semisoft elasticity and director reorientation in stretched sheets of nematic elastomers. *Phys. Rev. E.* **66**, 061710 (2002).
37. B. L. Mbanga, F. F. Ye, J. V. Selinger, R. L. B. Selinger, Modeling elastic instabilities in nematic elastomers. *Phys. Rev. E. Stat. Nonlin Soft Matter Phys.* **82**, 051701 (2010).
38. B. Yohsuke, K. Urayama, T. Takigawa, K. Ito, Biaxial strain testing of extremely soft polymer gels. *Soft Matter* **7**, 2632–2638 (2011).
39. A. J. Leadbetter, A. I. Mehta, Molecular packing in the nematic phase of cyano compounds with different ring systems. *Mol. Cryst. Liq. Cryst.* **72**, 51–57 (1981).
40. P. Cesana, P. Plucinsky, K. Bhattacharya, Effective behavior of nematic elastomer membranes. *Arch. Ration. Mech. Anal.* **218**, 863–905 (2015).
41. Y. Luo, J. Xing, Y. Niu, M. Li, Z. Kang, Wrinkle-free design of thin membrane structures using stress-based topology optimization. *J. Mech. Phys. Solids* **102**, 277–293 (2017).
42. M. O. Saed, A. H. Torbati, D. P. Nair, C. M. Yakacki, Synthesis of programmable main-chain liquid-crystalline elastomers using a two-stage thiol-acrylate reaction. *JoVE* , e53546 (2016).
43. T.-T. Mai, Y. Morishita, K. Urayama, Novel features of the Mullins effect in filled elastomers revealed by stretching measurements in various geometries. *Soft Matter* **13**, 1966–1977 (2017).
44. P. H. Hermans, P. Platzek, Beiträge zur Kenntnis des Deformationsmechanismus und der Feinstruktur der Hydratzellulose. *Kolloid-Zeitschrift.* **88**, 68–72 (1939).
45. J. S. Biggins, E. M. Terentjev, M. Warner, Semisoft elastic response of nematic elastomers to complex deformations. *Phys. Rev. E.* **78**, 41704 (2008).
46. H. Zhou, K. Bhattacharya, Accelerated computational micromechanics. *J. Mech. Phys. Solids* **153**, 104470 (2021).
47. P. Plucinsky, M. Lemm, K. Bhattacharya, Programming complex shapes in thin nematic elastomer and glass sheets. *Phys. Rev. E* **94**, 010701 (2016).
48. H. Aharoni, Y. Xia, X. Zhang, R. D. Kamien, S. Yang, Universal inverse design of surfaces with thin nematic elastomer sheets. *Proc. Natl. Acad. Sci. U.S.A.* **115**, 7206–7211 (2018).
49. J. Michel, H. Moulinec, P. Suquet, A computational method based on augmented Lagrangians and fast Fourier transforms for composites with high contrast. *Comput. Model. Engr. Sci.* **1**, 79–88 (2000).

Acknowledgments: We thank the Osaka Organic Chemical Industry Ltd. for the provision of the diacrylate compounds for the preliminary experiments and S. Okamoto for assistance in the experiments. **Funding:** K.U. is supported by JSPS KAKENHI grant number JP18H02034. K.B. and H.Z. are supported by the U.S. Air Force Office of Scientific Research MURI grant number FA9550-16-1-0566. **Author contributions:** K.U. conceptualized the experiment. K.B. provided theoretical insights for the experimental results. K.U. and K.B. supervised the project. H.T. and A.T. performed the sample preparation and mechanical tests. K.U., H.T., and A.T. analyzed the mechanical data. H.Z. carried out the full-field 3D simulation. K.Ka., K.Ko., and A.T. conducted the scattering experiments and the data analysis. K.U. and K.B. wrote the paper, and all of the authors edited the manuscript before submission. **Competing interests:** The authors declare that they have no competing interests. **Data and materials availability:** All data needed to evaluate the conclusions in the paper are present in the paper and/or the Supplementary Materials. Additional data related to this paper may be requested from the authors.

Submitted 24 September 2020
Accepted 5 May 2021
Published 18 June 2021
10.1126/sciadv.abe9495

Citation: H. Tokumoto, H. Zhou, A. Takebe, K. Kamitani, K. Kojio, A. Takahara, K. Bhattacharya, K. Urayama, Probing the in-plane liquid-like behavior of liquid crystal elastomers. *Sci. Adv.* **7**, eabe9495 (2021).